Check for updates

JGR Solid Earth

RESEARCH ARTICLE
10.1029/2020JB020177

Mantle Transition Zone Receiver Functions for Bermuda: Automation, Quality Control, and Interpretation

Alexander L. Burky[1], Jessica C. E. Irving[1,2], and Frederik J. Simons[1]

[1]Department of Geosciences, Princeton University, Princeton, NJ, USA, [2]School of Earth Sciences, University of Bristol, Bristol, UK

Key Points:

- We investigate the mantle transition zone structure below Bermuda using a new, automated, quality controlled receiver function approach
- The detected depression of the 660 km discontinuity beneath Bermuda is inconsistent with a whole-mantle plume in an olivine dominated mantle
- Alternatively, observed complexity around 660 km may indicate a hot through-going anomaly contingent on garnet's impact on the system

Supporting Information:

- Supporting Information S1

Correspondence to:
A. L. Burky,
aburky@princeton.edu

Citation:
Burky, A. L., Irving, J. C. E., & Simons, F. J. (2021). Mantle transition zone receiver functions for Bermuda: Automation, quality control, and interpretation. *Journal of Geophysical Research: Solid Earth*, *126*, e2020JB020177. https://doi.org/10.1029/2020JB020177

Received 15 MAY 2020
Accepted 10 DEC 2020

© 2020. American Geophysical Union. All Rights Reserved.

Abstract The origin of the Bermuda rise remains ambiguous, despite, or perhaps because of, the existence of sometimes incongruous seismic wave-speed and discontinuity models in the sub-Bermudian mantle. Hence, whether Bermuda is the surface manifestation of a mantle plume remains in question. Using the largest data set of seismic records from Bermuda to date, we estimate radial receiver functions at the Global Seismographic Network station BBSR in multiple frequency bands, using iterative time-domain deconvolution. Motivated by synthetic experiments using axisymmetric spectral-element forward waveform modeling, we devise a quality metric for our receiver functions to aid in the automation and reproduction of mantle transition zone discontinuity studies. We interpret the complex signals we observe by considering the mineralogical controls on mantle transition zone discontinuity structure, and conclude that our results are likely to be indicative of a thicker than average mantle transition zone. Our result is incompatible with the canonical model of a whole mantle plume in an olivine dominated mantle; however, considerations of phase transitions in the garnet system would allow us to reconcile our observations with the possible presence of a through-going hot thermal anomaly beneath Bermuda.

1. Introduction

Intraplate, or hot-spot, volcanism is typically interpreted as the result of plate motion over a spatially localized region of long-lived deep-mantle upwelling (Morgan, 1971). Arguably the most famous example of this process is the Hawaiian-Emperor Seamount Chain (e.g., Steinberger et al., 2004). Whether Bermuda belongs in this category of an intraplate volcano originating from a deep-mantle plume source remains uncertain. The island of Bermuda, situated atop a roughly 10^6 km^2 bathymetric swell in the Western Atlantic Ocean (Figure 1), lacks an age-progressive seamount chain and present-day active volcanism. Radiometric dating of borehole samples from the island and adjacent swell area revealed that the volcanic pedestal was formed during the Middle Eocene (ca. 48–45 Ma), and reached subaerial extent in the Late Eocene, approximately 40–36 Ma (Vogt & Jung, 2007). The pedestal has remained volcanically dormant since, and is now overlain by a fossiliferous carbonate platform. In spite of these facts, which suggest an isolated volcanic episode leading to Bermuda's formation, the region is included in some plume-hot-spot catalogs (King & Adam, 2014; Sleep, 1990), though it fails to meet others' definitions of a mantle plume (Courtillot et al., 2003) due to its lack of a hotspot track and weak evidence for a significant upper mantle low velocity anomaly from seismic tomography. Additionally, several studies suggest a link between the igneous activity which formed Bermuda and other volcanic events, such as the formation of the Mississippi Embayment (Cox & Van Arsdale, 2002; L. Liu et al., 2017) and the reactivation of the New Madrid rift system (Chu et al., 2013), though it may not be linked to all the magmatism along its purported track (Mazza et al., 2014).

Recent work in whole mantle seismic tomographic imaging has facilitated the observation and interpretation of several of these deep-mantle plume structures (e.g., French & Romanowicz, 2015), particularly in association with the Pacific and African LLSVPs (Lekić et al., 2012). The presence of a strong, high temperature mantle upwelling should be visible in tomographic images of mantle velocity. To explore this hypothesis in the context of Bermuda, we made cross sections through two seismic tomography models (Figure 2), the joint *P* and *S* velocity model LLNL_G3D_JPS (Simmons et al., 2015) and the radially anisotropic *S* velocity model SEMUCB_WM1 (French & Romanowicz, 2014). Both models display a low velocity anomaly beneath Bermuda relative to the one-dimensional (1-D) average velocity of the profile interrogated. This anomaly extends as a continuous feature to roughly 1,500 km depth, and then is deflected eastward (Figures 2b and 2c) by what appears to be the relict Farallon slab (Sigloch et al., 2008). In addition to a

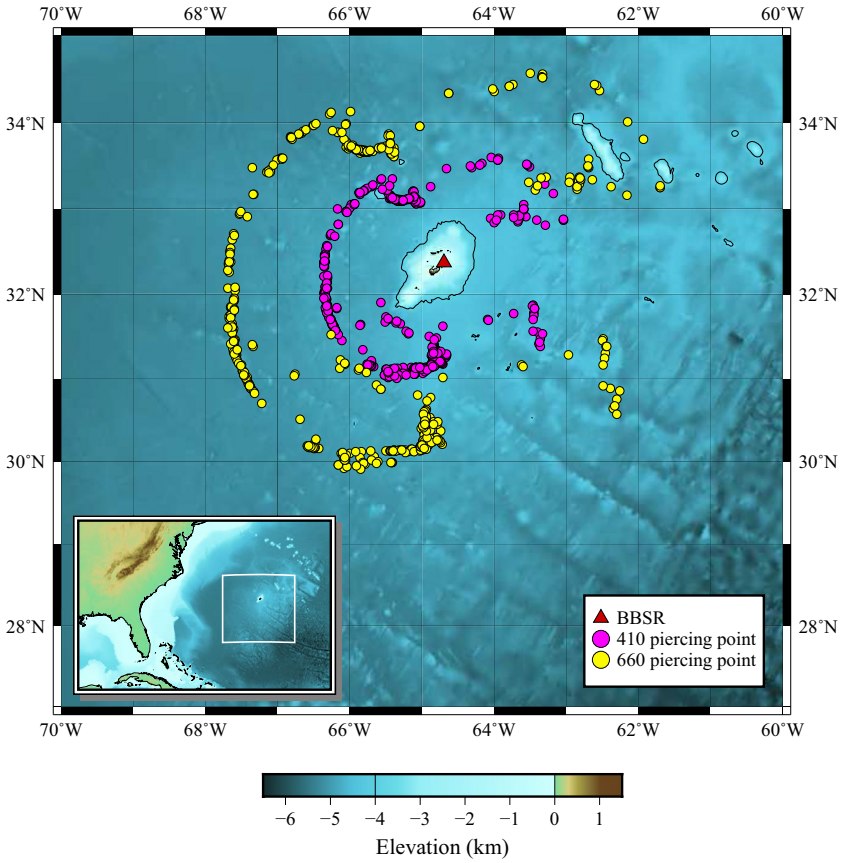


Figure 1. Bathymetry (Becker et al., 2009) of the study region, showing the location of Global Seismographic Network (GSN) station BBSR, and incoming *P410s* and *P660s* piercing points from the 226 earthquakes with high enough quality to be used in our receiver-function analysis. The bathymetric swell is roughly outlined by the 4 km depth contour. Note the absence of a well-defined hotspot track, which would be expected to trend East-West.

broad low velocity anomaly, both models show a localized low velocity anomaly of varying depth extent directly beneath Bermuda. This feature is observed most clearly in the North-South cross section through model LLNL_G3D_JPS (Figure 2e, directly beneath the central gray circle), and motivates our investigation. In model SEMUCB_WM1, this feature is pronounced at depths shallower than 410 km, and is faintly continuous through the mantle transition zone where it reaches maximum amplitude near 1,000 km depth (Figure 2f).

This paper has two objectives: (1) to assess the validity of the plume-hot-spot hypothesis for Bermuda using seismological techniques, specifically, by (2) developing a robust method to do so on a small (single-station) and noisy (island) data set. In this paper, we investigate the topography of the 410 and 660 km mantle discontinuities beneath Bermuda.

The mantle transition zone plays an important role in determining and revealing the behavior of mantle flow, and the topography of the seismic wave-speed discontinuities, at the nominal depths of 410 and 660 km (hereafter referred to as "the 410" and "the 660"), provides a proxy for the thermal and compositional state beneath a region (e.g., Helffrich & Wood, 2001). The 410 is understood to be controlled by the olivine to wadsleyite phase transition, an exothermic reaction at relevant pressure (P) and temperature (T) conditions, whose Clapeyron slope, dP/dT, is positive (Bina & Helffrich, 1994). The 660 is more complicated (Simmons & Gurrola, 2000; Vacher et al., 1998), due to the negative Clapeyron slope of the endothermic ringwoodite to bridgmanite and magnesiowüstite (ferropericlase) phase transition (Ito et al., 1990), and the positive Clapeyron slope of the exothermic majorite garnet to perovskite phase transition (Hirose, 2002). A "cold" mantle transition zone (e.g., one influenced by subduction) is expected to be thick. A "hot" mantle transition zone may have one of two different expressions: if it is a garnet-dominated system one would

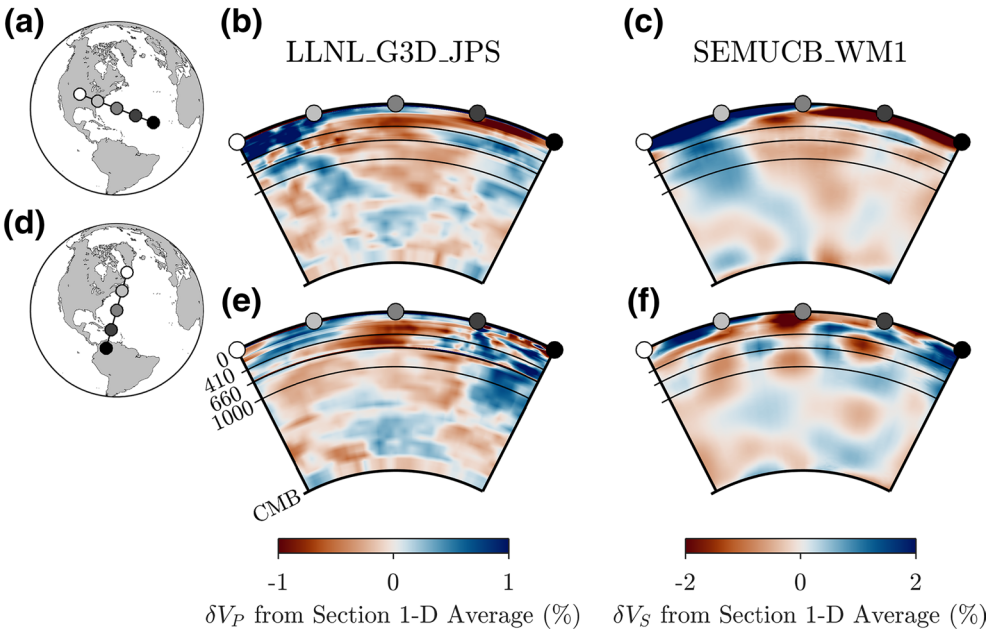


Figure 2. Cross sections centered on Bermuda through whole mantle tomography (b), (e) V_P component of model LLNL_G3D_JPS (Simmons et al., 2015) and (c), (f) V_S model SEMUCB_WM1 (French & Romanowicz, 2014). Wave speed perturbations are shown relative to the one-dimensional (1D) average velocity profile for the region shown in the cross section. Note the consistently imaged low seismic velocity anomaly extending through the mantle transition zone, but not necessarily through the entire mantle, beneath Bermuda. The anomaly is particularly apparent in the North-South cross sections (e) and (f).

expect simultaneous depression of both discontinuities (e.g., Jenkins et al., 2016). Alternatively, the more commonly expected situation is that a hot, olivine-dominated system should exhibit a thin transition zone, with a depressed 410 and an elevated 660 (Bina & Helffrich, 1994).

In order to characterize the 410 and 660 beneath Bermuda, we calculate radial receiver functions (Ammon, 1991; Langston, 1979; Ligorría & Ammon, 1999; Phinney, 1964; Vinnik, 1977) using earthquake data recorded on Global Seismographic Network (GSN) station BBSR. Using radial receiver functions calculated with the iterative time-domain deconvolution algorithm, Benoit et al. (2013) measured a 215 km thick mantle transition zone beneath BBSR. These authors then used the global average transition zone thickness of 242 km (Lawrence & Shearer, 2006) in conjunction with phase transition information to calculate the thermal anomaly implied by their measurement, arriving at a result of 172–320 K hotter than the reference model. In addition, their analysis of shear wave splitting revealed an isotropic (null splitting) upper mantle beneath Bermuda, which they interpreted as indicative of vertically upwelling mantle flow beneath the island. Another well documented study of the transition zone structure beneath Bermuda was performed by Gao and Liu (2014) as part of a larger investigation of the transition zone structure beneath the contiguous United States. Unlike Benoit et al. (2013), this study used a frequency-domain approach to calculate radial receiver functions for both *Pds* and *PPds* phases. Despite these differences, their study reaffirmed the results of Benoit et al. (2013), reporting a transition-zone thickness some 16 km thinner than the 250 km thickness of IASP91 (Kennett & Engdahl, 1991), mainly due to a depression of the 410 km discontinuity down toward ~440 km. In contrast to these two studies, Tauzin et al. (2008), using radial receiver functions calculated with the iterative time-domain deconvolution algorithm, found no notable thinning of the mantle transition zone under Bermuda. Instead, they reported a normal mantle transition zone thickness, albeit one with both the 410 and 660 deeper than the average at the stations they investigated. A key difference in the processing of each of these studies is their application of filtering; Benoit et al. (2013) performed no pre-filtering, Gao and Liu (2014) filtered all records between 5 and 50 s, and Tauzin et al. (2008) filtered all records between 10 and 25 s.

We build on these studies by including more recent waveform data, introducing a quantitative metric for classifying the quality of individual receiver functions, and by exploring the effects of different filtering

parameters on the resulting receiver functions. Our methodology therefore lends itself to providing a reproducible benchmark for future studies.

2. Data and Methods

We use teleseismic earthquake data from station BBSR in the Global Seismographic Network (network code IU). Several instruments have been operated at this station since its opening; we use the broadband channels (BH) with location ID 00. We requested seismograms from events with moment magnitudes $M_w > 5.5$ that occurred within an epicentral distance range of 30–90° from the station between August 2002 and November 2019 resulting in 1866 event records. We removed the appropriate instrument response from each seismogram, converting from digital counts to three-component displacement.

We are interested in isolating the conversions, due to impedance contrasts in the upper mantle beneath our station, of compressional wave energy into vertically polarized shear-wave energy. The three-component displacement record is

$$\mathbf{u}(t) = [u_Z(t) \quad u_N(t) \quad u_E(t)]^{\mathrm{T}}, \tag{1}$$

where the subscripts Z, N, and E refer to the vertical (up), north, and east components of motion in the local Cartesian coordinate system centered on the station. The particle motion of the P wave, and of the vertically (SV) and horizontally (SH) polarized shear waves is best expressed in a Cartesian coordinate frame relative to the seismic ray. We rotate the station components into the ray plane via the matrix transformation:

$$\begin{bmatrix} u_R(t) \\ u_T(t) \end{bmatrix} = \begin{bmatrix} \cos\theta & \sin\theta \\ -\sin\theta & \cos\theta \end{bmatrix} \begin{bmatrix} u_N(t) \\ u_E(t) \end{bmatrix}, \tag{2}$$

where $u_R(t)$ and $u_T(t)$ are now referred to as the radial and tangential displacement components, respectively, and θ is the azimuth at the station: the angle, measured clockwise from north at the station, to the extended great-circle arc directed from the earthquake epicenter to the recording station. The radial component of motion at the station is positive when directed away from the earthquake hypocenter. For the steep angles of incidence of teleseismic events, we make the assumption that $u_Z(t)$ contains the most important record of the P-wave motion and that $u_R(t)$ is most indicative of the SV-wave signal.

The final steps in our preprocessing are filtering and windowing (tapering) of the rotated seismograms. We analyze our results with no pre-filtering, and compare them to results using zero-phase filtering, utilizing a fourth-order, two-pass Butterworth filter with corner frequencies of 0.02 and 1 Hz, or 1–50 s period, respectively. Subsequently, we window the data around the calculated theoretical P arrival time in the IASP91 velocity model (Kennett & Engdahl, 1991), with the TauP-Toolkit (Crotwell et al., 1999), retaining data 30 s prior to and 90 s after this predicted time. We taper the seismograms using a Tukey window with cosine fraction 0.25. Examples of the resulting waveforms are shown in Figure 3, ready for use in studying the conversion of $u_Z(t)$ into $u_R(t)$ motion, or alternatively, of P into SV energy. For clarity and to aid in reproducing our results, we briefly summarize the theoretical basis for the Ligorría and Ammon (1999) analysis method that we employ.

2.1. Receiver Functions

Our modeling stipulates that the conversion between compressional (vertical-component) and vertically polarized shear (radial-component) motion is a linear time-invariant system (Bendat & Piersol, 2000), characterized by a convolutional ($*$) response, $f_{Z\to R}(t)$,

$$u_R(t) = (u_Z * f_{Z\to R})(t) = \int_{-\infty}^{\infty} u_Z(\tau) f_{Z\to R}(t-\tau) d\tau. \tag{3}$$

It is this response which we seek to determine and subsequently study as it relates to Earth structure. In the spectral domain, after forward Fourier transformation $\mathcal{F}$,

$$\tilde{u}_R(\omega) = \tilde{u}_Z(\omega)\tilde{f}_{Z\to R}(\omega), \quad \text{where} \quad \mathcal{F}(u) = \tilde{u} \quad \text{and} \quad \mathcal{F}(f_{Z\to R}) = \tilde{f}_{Z\to R}, \tag{4}$$

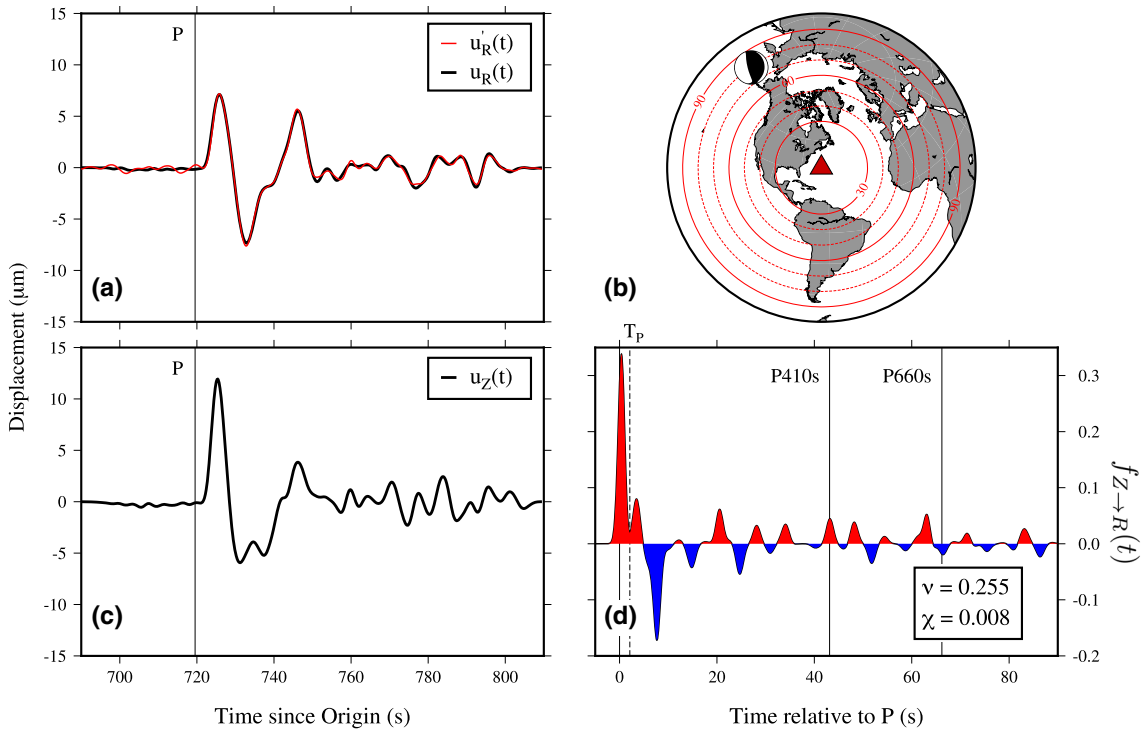


Figure 3. (a) Unfiltered radial and predicted radial (u_R and u_R') and (c) vertical (u_Z) component displacement seismograms recorded in Bermuda for the June 14, 2005 $M_W = 6.8$ earthquake at 53.9 km depth (C200506141710A). The vertical line shows the predicted *P* arrival time according to 1D velocity model IASP91. (b) Map showing the event with its corresponding Global Centroid-Moment-Tensor (CMT) focal mechanism (Ekström et al., 2012) solution. The red circles indicate different epicentral distances from BBSR. (d) Radial receiver function computed for this event using a Gaussian width factor $\tilde{\sigma} = 1.0$ Hz (see main text). The model quality factor, ν, and data misfit, χ, as discussed in the text, are included for reference.

and ω is the angular temporal frequency. Thus, in theory, the frequency-domain representation of the receiver function is recoverable by forming the ratio

$$\tilde{f}_{Z\to R}(\omega) = \frac{\tilde{u}_R(\omega)}{\tilde{u}_Z(\omega)}. \tag{5}$$

As written, Equation 5 is a solution without a practical method for achieving it (Langston, 1979). Of the many algorithms that have been developed to stably obtain an estimate of $f_{Z\to R}(\omega)$ from noisy, windowed, sampled data, we choose the iterative time-domain deconvolution approach of Ligorría and Ammon (1999), as detailed in the next section.

2.2. Iterative Time-Domain Deconvolution

Although the theoretical basis for the iterative time-domain deconvolution is in fact in the time-domain, algorithmic implementations, to our knowledge, very often rely on frequency domain operations. Here, we present a description of the algorithm as it operates in practice. In the following description, it is implied that characters with a tilde (e.g., $\tilde{u}_R(\omega)$) represent the discrete Fourier transform of time domain entities.

Contrary to the idealized scenario described in the previous section, the structural signal that we wish to recover from real seismic data is contaminated with noise. Therefore, in the discrete domain of noisily observed data, we model the system as

$$\tilde{u}_R(\omega) = \tilde{u}_Z(\omega)\tilde{f}_{Z\to R}(\omega) + \tilde{n}(\omega), \tag{6}$$

a version of Equation 4 contaminated by additive noise, $\tilde{n}(\omega)$, about which we make the minimal assumption that it is uncorrelated and incoherent with the signal, such that:

$$\langle \tilde{u}_Z(\omega)\tilde{f}_{Z\to R}(\omega)\tilde{n}^*(\omega)\rangle = 0, \tag{7}$$

where the angular brackets denote ensemble averaging and the star is used for the complex conjugate. Hence, from Equations 6 and 7, the system response, the theoretical quantity that we seek to recover, is then given by

$$\tilde{f}_{Z\to R}(\omega) = \frac{\langle \tilde{u}_R(\omega)\tilde{u}_Z{}^*(\omega)\rangle}{\langle \tilde{u}_Z(\omega)\tilde{u}_Z{}^*(\omega)\rangle}. \tag{8}$$

We reformulate the problem as one in which we wish to find, using a prime to denote an *estimate*, the $\tilde{f}'_{Z\to R}$ (or, in the time domain, $f'_{Z\to R}$) that, when multiplied (or convolved) with the observed vertical-component seismogram, $\tilde{u}_Z$ (or u_Z), produces an approximation to the radial component $\tilde{u}'_R$ (or u'_R) that is, sufficiently close to the observed $\tilde{u}_R$ (or u_R). The residual is denoted

$$\Delta\tilde{u}_R = \tilde{u}_R - \tilde{u}_R{}'. \tag{9}$$

Ligorría and Ammon (1999) formulated the time-domain solution iteratively as follows. We denote the iterates with a superscript, $\tilde{u}'^{(j)}_R$, $\Delta\tilde{u}^{(j)}_R$, and $f'^{(j)}_{Z\to R}(t)$, and initialize the process at iteration $j = 0$ using

$$\begin{cases} \tilde{u}'^{(0)}_R(\omega) &= 0, \\ \Delta\tilde{u}^{(0)}_R(\omega) &= \tilde{u}_R(\omega), \\ f'^{(0)}_{Z\to R}(t) &= 0. \end{cases} \tag{10}$$

Writing Δt for the time interval of the discretized sampling sequence of observations $n = 0, ..., N-1$, and introducing the notation

$$\| u_Z \|_2^2 = \Delta t \sum_{n=0}^{N-1} [u_Z(n\Delta t)]^2, \tag{11}$$

we proceed to determining, for iteration $j > 0$, the auxiliary quantities

$$\begin{cases} f_j(t) &= \mathcal{F}^{-1}\left\{\Delta\tilde{u}_R{}^{(j-1)}(\omega)\tilde{u}^*_Z(\omega)/\| u_Z \|_2^2\right\}, \\ t_j &= \arg\max\{f_j(t)\}, \\ F_j &= \max\{f_j(t)\}, \end{cases} \tag{12}$$

which we use to determine the jth receiver-function estimate as a train of Gaussians,

$$f'^{(j)}_{Z\to R}(t) = f'^{(j-1)}_{Z\to R}(t) + F_j\sigma\sqrt{2\pi}\, g(t;t_j,\sigma^2), \tag{13}$$

where $g(t; t_j, \sigma^2)$ is a Gaussian density function with an expectation t_j, as constrained by the data via Equation 12, and with a variance, σ^2, predetermined based upon bandwidth considerations at the onset, and held constant throughout the procedure. As defined here, σ is the time-domain version of what we call the "Gaussian width factor," which has as its frequency-domain counterpart,

$$\tilde{\sigma} = 1/\sigma, \qquad \text{the "Gaussian width factor".} \tag{14}$$

We recognize $f_j(t)$ in Equation 12 as a time-domain equivalent of Equation 8, without the averaging brackets, and replacing the effect of the denominator, via Parseval's theorem, by the mean-squared energy $\| u_Z \|_2^2$ computed in the time-domain as introduced in Equation 11. The expression (13) matches the maximum amplitude, F_j, of the intermediate quantity $f_j(t)$ at the location of its peak, t_j.

The evolving receiver-function estimate $f'^{(j)}_{Z\to R}(t)$ is applied to the unchanged vertical-component data $u_Z(t)$ by frequency-domain multiplication to form the evolving radial-component prediction. This prediction is then transformed back into the time domain and subtracted from the original data $u_R(t)$ to define the updated residual

$$\Delta u_R{}^{(j)}(n\Delta t) = u_R(t) - \mathcal{F}^{-1}\left\{\tilde{f}'^{(j)}_{Z\to R}(\omega)u_Z(\omega)\right\}, \tag{15}$$

which re-enters Equation 12 at each iteration.

As the iterations proceed, we monitor the quality of the fit via the fractional energy of the residual in 15, compared to the observed radial-component displacement record, again in the time-domain, as

$$\chi_j = \frac{\sum_{n=0}^{N-1}[\Delta u_R{}^{(j)}(n\Delta t)]^2}{\sum_{n=0}^{N-1}[u_R(n\Delta t)]^2}. \tag{16}$$

We iterate over Equations 12–15, counting $j = 1, ..., J$, until the change of misfit χ_j in subsequent iterations is smaller than some predefined tolerance,

$$\Delta\chi_j = \chi_j - \chi_{j-1} < \varepsilon. \tag{17}$$

We use a value of $\varepsilon = 10^{-5}$, and impose the additional constraint that the total number of iterations be limited to $J \le 1{,}000$. See Figure 3 for an illustration summarizing the algorithm.

The time-domain receiver-function estimate is $f'^{(J)}_{Z\to R}$, or $f'_{Z\to R}$, for short, and its associated data misfit is χ_J, or simply χ in what follows.

2.3. Automating Receiver Function Quality Control

Now that we have fully documented our method for producing receiver functions, we describe our methods for assessing their quality for our primary objective of resolving the discontinuity structure of the mantle transition zone beneath our station. Although χ, the fractional residual at the final iteration, quantifies the quality of a receiver function $f'_{Z\to R}$ in its performance solving Equation 6 for the unknown true $f_{Z\to R}$, it provides neither insight nor control on the quality of the seismograms fed into the deconvolution algorithm (for this, see also Yang et al., 2016), nor does it factor in any prior notion of what a "good" receiver function should resemble. To account for these considerations, we impose three quality control criteria: one on the input seismograms, and two on the output receiver functions.

The first measure of quality, imposed on the input seismograms, is the signal-to-noise ratio (SNR) of $u_Z(t)$ and $u_R(t)$. We use the method outlined in Gao and Liu (2014), where the SNR is defined as $\max|A_s| / |\overline{A_n}|$, where $\max|A_s|$ is the maximum absolute value of the record over the interval ranging from 8 s before to 12 s after the predicted arrival time of P in the IASP91 model, and $|\overline{A_n}|$ is the mean absolute value of the record between 20 and 10 s before the predicted P arrival time. We only accept input data with SNR ≥ 4.

The second measure of quality, and the first imposed on the receiver functions themselves, is on the data misfit χ (Equation 16). We accept receiver functions which yield a final value of $\chi \le 0.2$, or equivalently, where convolution of the u_Z data with the receiver function estimate $f'_{Z\to R}$ produces a final fit to the u_R data that is 80% or greater in terms of energy.

Our third and final measure of quality is a metric designed to quantify the shape or distribution of information within the receiver function. Forward modeling experiments that we conducted using 1D reference model IASP91 with the spectral-element wave-propagation code AxiSEM (Nissen-Meyer et al., 2014) showed that a "good" receiver function produced using the Ligorría and Ammon (1999) algorithm described in the previous section will display its largest amplitude spike at time zero, corresponding to the incident P wave arrival. Subsequent spikes have smaller amplitudes, representing the longitudinal-to-shear *Pds* phases converted at discontinuities at depths d km, and their surface and internal reverberations. Significant departures from this characteristic shape or figure-of-merit can be caused by noisy input records and phases interfering in the P wave coda, such as the surface reflection *PP* at epicentral distances smaller than 35° and the core-reflected phase *PcP* in the epicentral distance range 50°–60°. It is, therefore, reasonable to demand that a "good" receiver function show a large Gaussian pulse due to the incident P wave arrival, compared

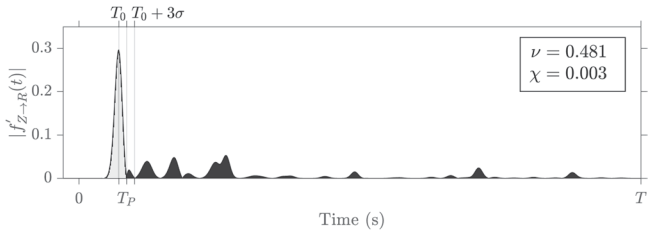


Figure 4. Illustration of our quality control metric, ν, on a synthetic receiver function made in model IASP91 using AxiSEM. Synthetics were calculated for a $M_w = 6.0$ event, at 20 km depth. The receiver function shown corresponds to the recorded displacement 52° away from our synthetic event. The metric weights the main P arrival relative to the P wave coda. The Gaussian width $\tilde{\sigma} = 1.0$ Hz, and the length of the window considered, $T = 120$ s. The light gray shaded area corresponds to the numerator in Equation 18.

to any other subsequent Gaussian pulses in the receiver-function coda. These considerations motivate us to define a quality control metric as

$$\nu \equiv \frac{\int_0^{T_P} f'_{Z\to R}(t)dt}{\int_0^{T} |\, f'_{Z\to R}(t)\,| dt}, \qquad \nu \in [-1,1], \tag{18}$$

where T is the length of the entire time window under consideration, and T_P is defined as the smallest of the set of times t whereby the receiver function or its first derivative vanish, within a restricted window of length 3σ after T_0, at which the receiver function $f'_{Z\to R}(t)$ reaches its maximum value due to the incident P wave,

$$T_P = \min\left[\left\{t : f'_{Z\to R}(t) = 0\right\}, \left\{t : \frac{df'_{Z\to R}(t)}{dt} = 0\right\}\right] \quad \text{for} \quad t \in \left[T_0, T_0 + 3\sigma\right], \tag{19}$$

where $\sigma = \tilde{\sigma}^{-1}$ is the temporal Gaussian width factor defined in Equation 14. By this definition we effectively isolate the earliest major pulse in the receiver function. See Figure 4 for an illustration. Large values of ν correspond to "good" receiver functions while small values of ν correspond to receiver functions with "ringy" P wave codas (Figure 5).

We note that this criterion might be unhelpful in those cases where the presence of a low-velocity layer or complex crustal structure causes receiver functions to be very oscillatory (Yu et al., 2015; Zelt & Ellis, 1999). In such cases, we suggest that the distribution of ν values may reflect the presence of such structure. At present, we believe this metric, as used in this paper, is best suited for studying mantle transition zone structure beneath stations installed on bedrock. Further investigation of its characteristics in a variety of geologic environments will help to develop an understanding of its strengths and limitations in aiding receiver function studies of the subsurface. Finally, we emphasize that in addition to effectively filtering "bad" receiver functions from our dataset, our metric ν provides an easily implementable, reproducible, and objective measure of receiver function quality which can be incorporated into a data analysis workflow.

We are certainly not the first group to attempt to automate the calculation of receiver functions, and those interested in the subject are likely familiar with the existing EarthScope Automated Receiver Survey (EARS) product (Crotwell & Owens, 2005), which performs automated analysis of crustal structure using receiver functions. The key difference between our method and EARS is that they limit their quality control criterion to a SNR consideration and a deconvolution fit consideration. In addition, since they are interested in investigating the crust they use a higher value of $\tilde{\sigma} = 2.5$ for their Gaussian width factor. Our method allows for a similar automation procedure for mantle transition zone receiver functions, but also improves upon it by introducing an additional measure on the quality of individual receiver functions, ν.

2.4. Time-To-Depth Conversion

The final step in our workflow involves the conversion of the obtained receiver functions from the time domain into the depth domain. In order to achieve this mapping, we must assume a velocity model which allows us to associate times of specific pulses in our receiver functions with *Pds* conversion depths d, thereby also correcting for the temporal moveout of the *Pds* phases due to the spread of event-station distances in our data (Gurrola et al., 1994; Kind & Vinnik, 1988). For a 1D Earth model, following Chevrot et al. (1999) and others, the conversion is performed using the approximate expression

$$t_{Pds}(p,z) = \int_0^Z \left[\sqrt{V_S^{-2}(z) - p^2 r^{-2}} - \sqrt{V_P^{-2}(z) - p^2 r^{-2}}\right] dz, \tag{20}$$

where p represents the P wave ray parameter (s/km) of the receiver function being converted, $r \in [0, 1]$ is the ratio of the discontinuity radius to the Earth radius for a candidate discontinuity at a particular depth Z,

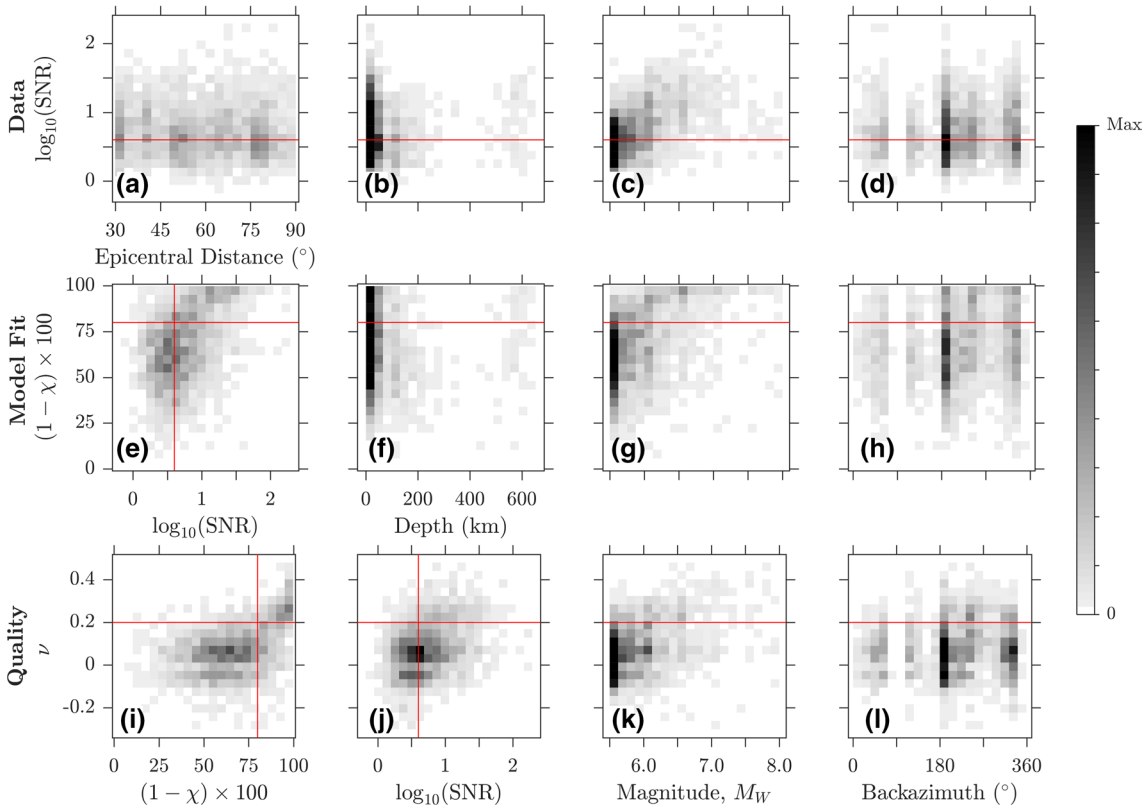


Figure 5. Summary of data and model quality statistics for the 1,866 events and their corresponding radial receiver functions. Threshold values used in the automated quality control selection are shown by the red lines. White denotes the absence of data density in a given bin, whereas black denotes maximum data density. Of particular interest are the relations between the vertical component data SNR, convolutional model fit, and receiver function quality parameter, ν (panels e, i, and j). Where axis labels are absent it is implied that the plot shares an axis label with the plots below it or the plots to its left.

and $V_P(z)$ and $V_S(z)$ are the P and S wave speed profiles as a function of depth, z. The integral in Equation 20 is computed at $\Delta z = 1$ km intervals in depth from 0 to 800 km to map time t to Pds conversion depth Z. We work with the 1D velocity model IASP91, so as to provide a more direct comparison of our results to those of Gao and Liu (2014). Once these moveout times were calculated, we depth-converted and stacked all of our accepted receiver functions in the following manner (K. H. Liu & Gao, 2006),

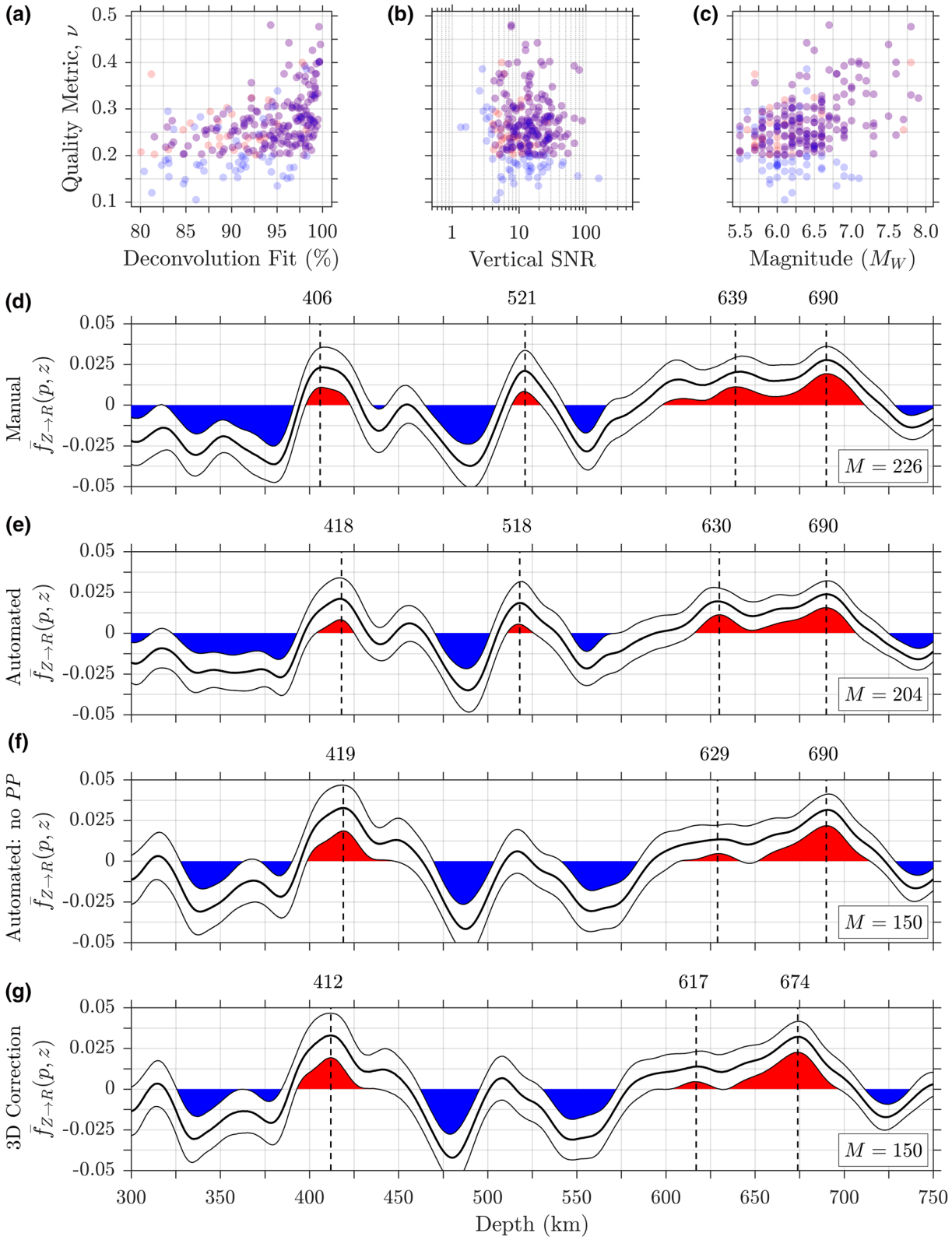
$$\overline{f}_{Z\to R}(p,z) = \frac{1}{M}\sum_{m=1}^{M} f'^{m}_{Z\to R}\left(t^{m}_{Pds}[p,z]\right), \tag{21}$$

where $\overline{f}_{Z\to R}(p,z)$ is the amplitude of the stack as a function of depth z and ray parameter p, M is the number of receiver functions, $t^{m}_{Pds}[p,z]$ is the moveout time for the mth receiver function as a function of depth, z, for the ray parameter p corresponding to the given event, and $f'^{m}_{Z\to R}\left(t^{m}_{Pds}[p,z]\right)$ is the amplitude of the mth receiver function at time $t^{m}_{Pds}[p,z]$, the moveout time calculated in Equation 20.

In addition to depth converting receiver functions using the 1D velocity model IASP91, we performed 3-D depth corrections using the joint P and S velocity model LLNL_G3D_JPS. To do this, we ray traced individual paths through the model for each of our selected events. Using the P and S velocity profiles calculated for each path, we solved Equation 20 to associate times with conversion depths in each receiver function. We subsequently stacked these receiver functions using Equation 21.

To estimate standard deviations for our stacked receiver functions, we applied the bootstrap resampling procedure (Efron & Tibshirani, 1986), where stacks are generated using a random subset of the receiver-function data. This resampling was carried out 1,000 times.

Finally, to establish confidence in our methodology and to build an intuition for our ability to resolve the mantle transition zone discontinuities, we applied our methods to a set of 2 Hz synthetic data. We calculated


(a)
Quality Metric, ν
Deconvolution Fit (%)
(b)
Vertical SNR
(c)
Magnitude (M_W)
(d)
Manual
406
521
639
690
$M = 226$
(e)
Automated
418
518
630
690
$M = 204$
(f)
Automated: no PP
419
629
690
$M = 150$
(g)
3D Correction
412
617
674
$M = 150$
$\bar{f}_{Z\to R}(p,z)$
Depth (km)

synthetics using the web-based Syngine tool (van Driel et al., 2015), using the event depths, locations, and CMT solutions of our dataset. The results of this experiment gave us confidence that our method worked, and can be found in Figure S1.

3. Results

We are now equipped to begin viewing the mantle transition zone discontinuity structure beneath Bermuda through the lens outlined above. Our observations are directly influenced by the choices of parameters we use to construct them; therefore, we systematically catalog the behavior of our observations as functions of these parameters. First, we compare the performance of our automated quality control metric, ν, to a control experiment conducted manually. We then explore the influence of interference from the surface reflected phase *PP* on our receiver function data. Third, and finally, we investigate the behavior of our results as a function of the pre-filtering applied to the seismograms. This analysis elucidates some of the nuances of the receiver function method in general, and additionally informs us about the nature of the mantle transition zone beneath Bermuda.

3.1. Comparison of Manual and Automated Data Selection

To benchmark our automated quality control metric against a hand-picked receiver function workflow, we manually selected high quality receiver functions from our dataset calculated with a Gaussian width $\tilde{\sigma} = 1.0$ Hz. A receiver function was accepted if it had a large, positive polarity first arrival, no monochromatic or "ringy" oscillations, and no negative-polarity arrivals of greater magnitude than the first arrival in the receiver function. In addition, we only considered receiver functions which resulted in a data fit $(1 - \chi) \times 100 \geq 80\%$. This process resulted in the selection of 226 receiver functions, which were then depth-converted and stacked according to the procedure outlined in Section 2.4. The resulting stack and accompanying statistics for this data set are shown in Figure 6. We note that this data set has our quality metric ν ranging between 0.1 and 0.5. This suggests that this metric may successfully be capturing the features which receiver function practitioners typically associate with high-quality receiver functions.

Next, we repeated the receiver function stacking procedure, but this time we automated the quality control process by selecting only receiver functions with a fit greater than 80%, a signal-to-noise ratio, SNR ≥ 4, and quality metric $\nu \geq 0.2$. This value of ν was chosen based on finding that all of our synthetic data had $\nu > 0.3$. We subsequently adjusted this value down until we arrived at a suitable cut off in terms of the number of receiver functions retained. In all, 204 receiver functions met these criteria. The resulting automated stack bears a close resemblance to the manual one, aside from slight shifts in the depths corresponding to the maximum peaks in the stacks. Additionally, both methods preserve the complex nature of the 660 km discontinuity.

Inspection of the automated and manual stacks reveals a consistent signal associated with the 520 km discontinuity ("the 520") beneath Bermuda. Initially, we found this to be an interesting feature, potentially bearing compositional implications. Further probing of the dataset, however, revealed that this feature is less significant, being magnified by contamination of receiver functions in the 30°–35° distance range by the *PP* phase. This is shown in Figure 7, where we analyzed our receiver functions as a function of epicentral distance to see if arrivals had the correct moveout (Dueker & Sheehan, 1997; Helffrich et al., 2003), and was subsequently verified by synthetic experiments. After accounting for this contamination by removing receiver functions from earthquakes with epicentral distances below 35°, the imprint of the signal associated with the 520 km discontinuity diminished (Figure 6f).

To explore the effects of 3D heterogeneity on our result, we performed the same process but chose to depth convert our receiver functions using model LLNL_G3D_JPS. The resulting stack, taking into account 3D ef-

Figure 6. (a)–(c) Quality control statistics. Filled red dots correspond to the data selected by the automatic algorithm, light blue dots correspond to data selected by manual inspection, and purple dots correspond to data selected by both methods. (d) Manual, (e) automated, (f) automated after removal of *PP*, and (g) automated after removal of *PP* with 3D depth correction receiver function stacks. The stacks are made from receiver functions with no pre-filtering, computed using a Gaussian width factor $\tilde{\sigma} = 1.0$ Hz. The bold central line is the bootstrapped mean, and the thin upper and lower lines represent bootstrap estimates of two standard deviations about the mean. The dashed vertical lines indicate the locations of relevant maxima with the corresponding depths annotated above each plot. Note the general agreement between the automated and manual results.

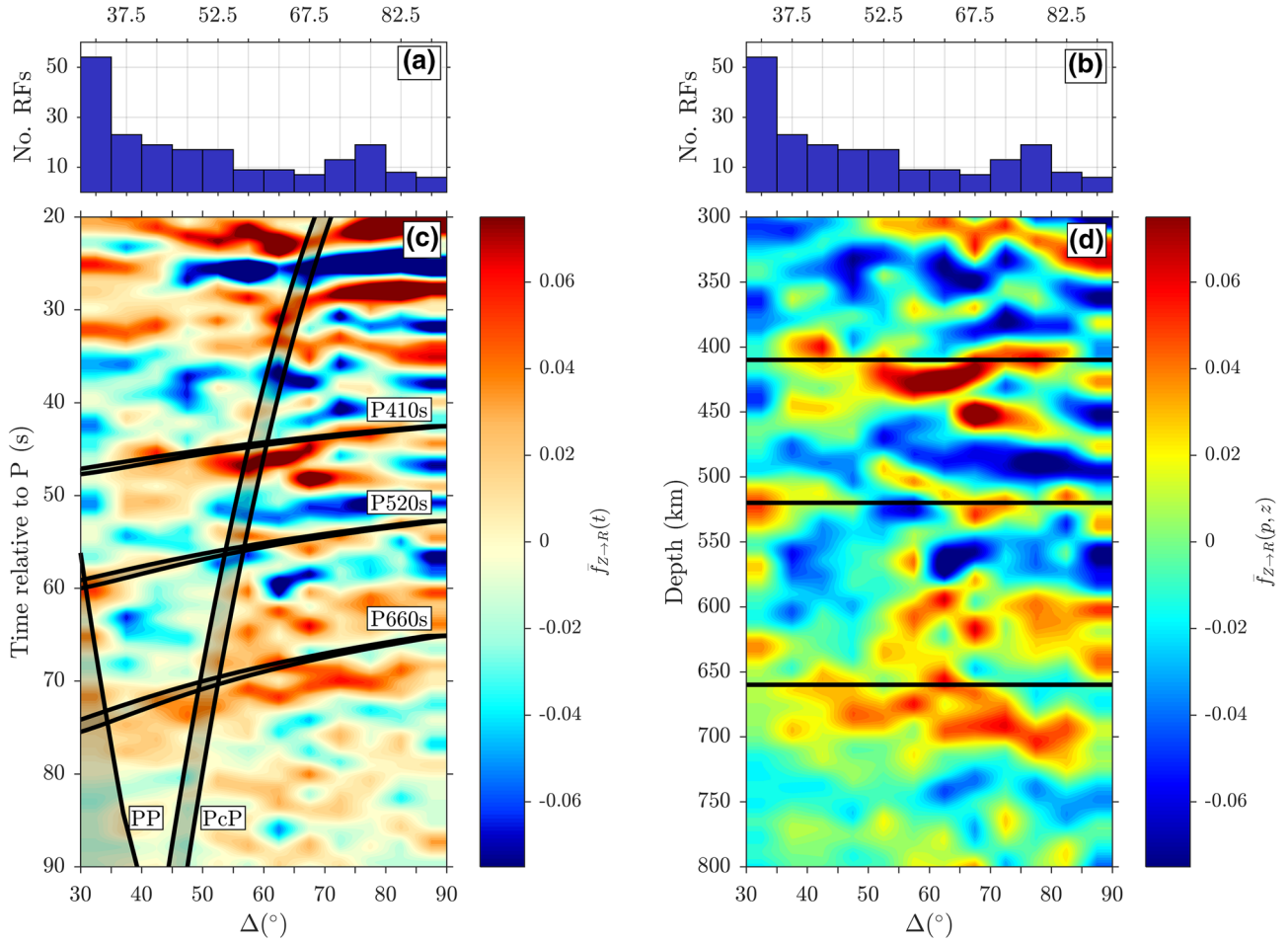


Figure 7. (a)–(b) Identical histograms showing the distribution with epicentral distance of the receiver functions that went into the construction of the panels below them. (c) Time-domain receiver functions arranged by epicentral distance. Binning is in 5° increments starting at 30°. Shaded gray regions indicate theoretical arrival times of *PP*, *PcP*, and relevant *Pds* phases from the mantle transition zone calculated using IASP91 according to Equation 20, for a range of earthquake depths between 0 and 653 km. Note the large signal from *PP* in the 30°–35° bin, with a similar arrival time to *P520s*. (d) Depth-domain receiver functions, moveout-corrected using 1D model IASP91. The 410 appears depressed, with a prominent signal between 50 and 80°, but the resolution of the depth of the 660 is poor, as it appears to occur over a broader depth range.

fects, the absence of *PP*, and using a fully automated quality control method, is shown in Figure 6g. We find that the 3D depth correction has the effect of shifting the peaks associated with the mantle transition zone up to shallower depths, while also slightly decreasing the observed transition zone thickness from 271 to 262 km. The shifting of arrivals to shallower depths is largely due to a more accurate, thin, crustal structure, which shifts all arrivals to earlier times due to traveling a greater distance at higher mantle velocities. Aside from these slight shifts, the overall shape of the result is remarkably similar to Figure 6f.

3.2. Frequency Dependence of Results

The filter chosen when preprocessing the seismic data exerts an influence on our final results (see also Leahy, 2009). In the stacks presented in Figure 6, no pre-filtering was performed. To explore the effect of filtering, we chose to pre-filter the data using a variety of pass-bands before proceeding to calculate receiver functions. The filter that we used was a fourth-order, two-pass Butterworth filter with corner frequencies at 0.02 and 1 Hz. The long-period corner of this filter was decremented in 1 s intervals, from a starting period of 50 s down to a final period of 2 s. After filtering, we calculated receiver functions using a Gaussian width factor $\tilde{\sigma} = 1.0$ Hz, and depth-converted and stacked using 1D model IASP91 following the methodology outlined above. Earthquakes with epicentral distances smaller than 35° were discarded from the stacks.

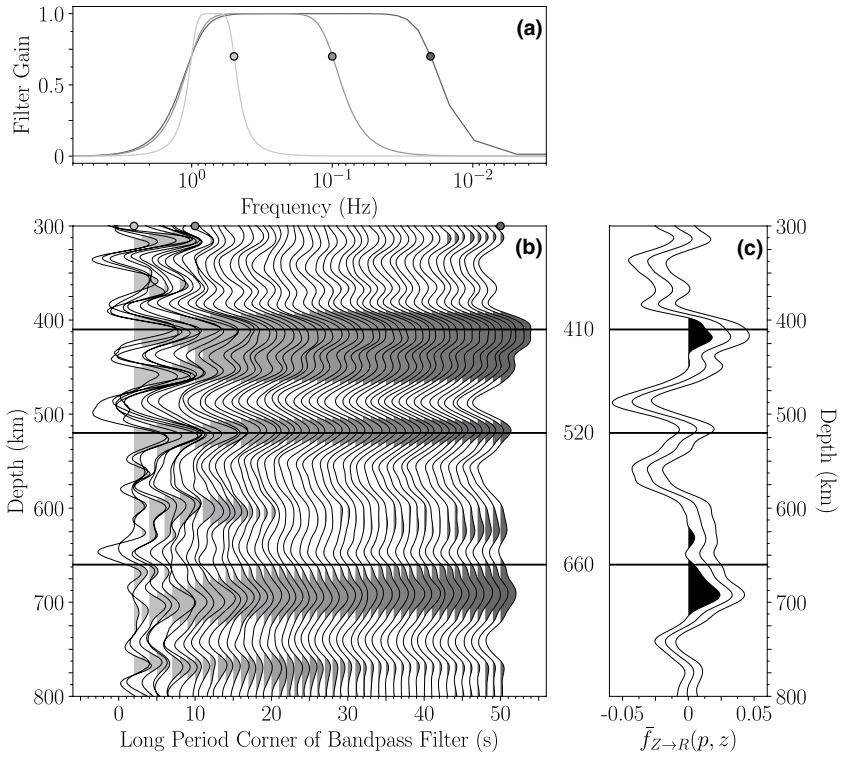


Figure 8. The effect of pre-filtering on receiver function stacks, using (a) a narrowing bandpass filter. (b) Depth-converted and stacked receiver functions as a function of the long-period corner of the bandpass filter used to pre-filter seismograms, alongside (c) the unfiltered, automated stack from Figure 6f for comparison. The short period corner is fixed at 1 s. Positive areas are colored gray, with the shading indicating the sense of the narrowing bandpass filter (a) depicted above. Note the frequency dependence of the 660 km discontinuity, which weakens at short periods, and the splitting of the peaks near 410 km into distinct peaks at short periods. Additionally, the presence of the 520 despite removal of records with *PP* interference is noteworthy, although the prominence of this signal may be exaggerated by the absence of bootstrap standard deviations.

The results of this experiment are displayed in Figure 8. Relatively high-frequency receiver functions can be found on the left-hand side of Figure 8b, and relatively low-frequency receiver functions to the right. Examples of the filter bandwidths are shown in Figure 8a, with shading corresponding to the receiver functions in Figure 8b. For comparison, Figure 8c is a copy of the receiver function previously shown in Figure 6f.

The 410 and 660 are observed across the entire range of frequencies shown. The depths of the discontinuities are consistent with the results shown in Figure 6, giving us additional confidence in their robustness. A particularly noteworthy feature is the double-peaked nature of the 410, which separates into two independent peaks at higher frequencies. Additionally, we observe a strong frequency dependence of the shallower signal in the vicinity of the 660. This observation suggests that the deeper peak observed at 674 km in our 3D depth corrected stacks, which is consistently observed across the range of frequencies we tested, corresponds to the 660. The shallower peak at 617 km, despite appearing statistically significant in our 3D depth corrected stacks (Figure 6g), appears to be a strongly frequency dependent feature.

Surprisingly, the 520 appears to be consistently imaged when the seismic data are pre-filtered. This result was unexpected, seeing as we excluded data from events with epicentral distances smaller than 35° in order to avoid interference from the *PP* phase. The visibility of this feature may be slightly exaggerated in Figure 8 compared to Figure 6f, where it is not statistically significant at the 2σ level, due to the absence of the uncertainties associated with the bootstrap resampling. Its relative prominence in the frequency bands chosen may also be indicative of the spectral characteristics of the discontinuity—perhaps it is a longer-wavelength, broader feature which is best observed at longer periods. This would be consistent with mineralogical understanding of the 520 as a broader discontinuity than the 410 or 660 (e.g. Tsujino et al., 2019).

To better constrain our observations, we produced slowness stacks, or vespagrams (Cottaar & Deuss, 2016; Davies et al., 1971), of our results to determine whether or not they showed arrival times and slownesses consistent with the *Pds* phases of interest. The results of this experiment are included in Figures S2 and S3 of the supplement. The vespagrams show that the main 410 arrival and deeper 660 arrival appear consistent with the predicted arrival times and slownesses of *P*410*s* and *P*660*s*. The secondary peak after 410 has a positive slowness, and is thus not likely related to the 410 km discontinuity. The small peak before 660 appears broad and poorly focused in the vespagram, and thus remains difficult to classify. Additionally, there is a positive slowness arrival which contributes to this peak, which further clouds our ability to assert its robustness. We also found that the arrival from the 520 appears to have the correct slowness and arrival time of *P*520*s*, even after excluding events with epicentral distances smaller than 35°.

In addition to this experiment, we also performed the complimentary experiment of varying the short-period corner of the filter used from 1 s up to 50 s. The effects of this alternative series of filters were less revealing, and we found that the 410 remained visible up to periods of 25 s while the 660 was quickly suppressed at periods beyond 10 s. This suggests that the 410 may be a broader feature, an observation typically associated with water in the transition zone (van der Meijde et al., 2003), while the 660 is sharper. The results of this experiment can be found in Figure S4.

Lastly, we explored the effect of the Gaussian width factor used in the iterative time-domain deconvolution. We progressively incremented the Gaussian width factor used from 0.5 to 1.0 with a step size of 0.05, and depth converted and stacked the resulting receiver functions. The 410 and 520 remained observable and largely unchanged by this procedure, but the 660 showed some variation. At low Gaussian width factors the distinct peaks observed near 660 became indistinguishable, and progressing to higher Gaussian width factors caused them to separate out into two distinct peaks. These results are shown in Figure S5.

4. Discussion

Our results suggest a considerably different picture of the mantle transition zone beneath Bermuda than the previous work of Benoit et al. (2013) and Gao and Liu (2014). Contrary to the strong depressions of the 410 observed by those authors, we only observe a modest 2 km depression of the 410–412 km depth, and we consistently observe a prominent signal from the 660 at a depth centered on 674 km, as shown in our 3D depth corrected stack (Figure 6g). These measurements are indicative of a slightly thicker than average mantle transition zone beneath Bermuda, at 262 km thick. Although this result is not readily compatible with the idea of a whole-mantle plume beneath Bermuda, previous work has also suggested poor correlation of receiver function imaged thinned transition zones with candidate hotspot locations (Tauzin et al., 2008).

4.1. Estimation of a Thermal Anomaly

Using our depth-converted and stacked receiver functions, we can make an estimate of the transition-zone thickness beneath station BBSR to use as a proxy for determining the temperature anomaly from the global average. We use the following equation from Helffrich (2000) to calculate this anomaly for our calculated transition-zone thicknesses,

$$z = z_0 + \delta T\left(\frac{dz}{dP}\right)\left[\left(\frac{dP}{dT}\right)_{660} - \left(\frac{dP}{dT}\right)_{410}\right], \tag{22}$$

where z represents observed transition-zone thickness, and $\left(dP\,/\,dT\right)_{660}$ and $\left(dP\,/\,dT\right)_{410}$ are the Clapeyron slopes of the ringwoodite to bridgmanite and magnesiowüstite (ferropericlase) phase transition, and the olivine to wadsleyite phase transition, respectively. Following Akaogi et al. (2007), we use values of $\left(dP\,/\,dT\right)_{660} = -2.6$ MPa/K and $\left(dP\,/\,dT\right)_{410} = 3.1$ MPa/K in our estimation, and following Benoit et al. (2013), a value of $z_0 = 242$ km (Lawrence & Shearer, 2006) for our global average transition-zone thickness.

4.2. Assessment and Interpretation of Discontinuity Structure

If we take the common approach of assuming that we are only observing the ringwoodite to bridgmanite and magnesiowüstite phase transition at the base of the transition zone in our dataset, then we choose the peak at 674 km to be representative of this transition, as it is the dominant signal across all frequencies. Using an observed value of $z = 262$ km (Figure 6g), results in a temperature anomaly of $\delta T = -137$ K for the mantle transition zone beneath Bermuda relative to the global average. This result is inconsistent with the presence of a hot thermal anomaly at depth beneath Bermuda in an olivine dominated mantle.

Alternatively, a second interpretation, more consistent with the idea of a hot thermal anomaly, can be justified if we consider garnet. Work by Hirose (2002) revealed that majorite garnet, a potentially major mantle constituent mineral, transforms into an aluminum bearing perovskite near 660 km depth. In addition, this phase transition is associated with a positive Clapeyron slope, meaning that the transition depth increases with increasing temperature.

Unfortunately, we cannot simply adapt Equation 22 to estimate the temperature anomaly taking this garnet phase transition into account. If we attempt to replace $\left(dP\,/\,dT\right)_{660}$ with $\left(dP\,/\,dT\right)_{maj.}$, the Clapeyron slope of the majorite garnet to perovskite phase transition, we find that, due to the large positive value of $\left(dP\,/\,dT\right)_{410}$, whether temperature is positively or negatively correlated with relative thickness depends on the chosen value of $\left(dP\,/\,dT\right)_{maj.}$. The appropriate value to choose for this slope is uncertain (Jenkins et al., 2016). We also do not have a good estimate for the appropriate value of z_0 for a region where the garnet system dominates. Thus we cannot extract a temperature estimate from our observations of transition zone thickness. Nonetheless, the presence of a complex 660 and the suggestion of a hot upper mantle from tomography lend some credence to this second interpretation.

Previous receiver function studies have observed similarly complex structure on the 660 and have attributed it to majorite garnet (Andrews & Deuss, 2008). In addition, investigations using *PP* (Day & Deuss, 2013; Deuss et al., 2006) and *SS* (Houser & Williams, 2010) precursors have revealed the presence of reflections from below 660 km consistent with this interpretation. Taking these factors into consideration suggests that we may be observing a hot thermal anomaly beneath Bermuda, consistent with previous results and the idea of a whole mantle plume penetrating the mantle transition zone beneath Bermuda.

We can quantify the magnitude of such a potential hot anomaly using the tomographic models shown in Figure 2. Using observed seismic velocities, we can produce an estimate of the relevant temperature anomaly (Cammarano et al., 2003). From Figure 2, we find a $\delta V_P = -0.5\%$ and a $\delta V_S = -0.5\%$, which correspond to a roughly +100 K temperature anomaly in the transition zone beneath Bermuda. We note here that damped tomographic inversions often underestimate the amplitude of velocity anomalies (e.g., French & Romanowicz, 2014), which suggests that this tomography-derived estimate is a lower bound on the real value.

It is also worth commenting on our observation of a discontinuity near 520 km depth. The 520 is discounted as a global feature in most seismic reference models, but is thought to arise from the wadsleyite to ringwoodite phase transition (Frost, 2008). Previous studies of the mantle transition zone beneath Bermuda failed to observe a signal from the 520, but as shown by Figures 6 and 8, it can be observed although it is clearly frequency dependent. The presence of signal from the 520 at longer periods is consistent with a previous study by Shearer (1990), where long-period *PP* and *SS* data were used. Although we are using converted rather than reflected seismic phases in our analysis, our results appear to be consistent with theirs in the 1–50 s period range. Further analysis of receiver function data at these periods will prove interesting, and could give greater insight into the global nature of the 520 km discontinuity.

5. Conclusions

We have introduced an automated and objective measure of receiver function quality that is simple to implement and tune. Using this measure produces results consistent with those typically sought when studying the mantle transition zone with receiver functions. We applied our technique to a geologically interesting location, and found results which shed new light onto the complexity of the mantle transition

zone beneath Bermuda. The choice of parameters used when conducting a receiver function study can have a great deal of influence on the final result and interpretation. Considering only phase transitions in the olivine system, our results suggest a thicker than average, 262 km thick mantle transition zone reflecting a cold thermal anomaly of −137 K beneath Bermuda. Such a result was unexpected. Alternatively, considering phase transitions of garnet may lead to another possible interpretation of our observations, suggestive instead of a hot (+100 K) thermal anomaly, contingent upon this transition's presence, importance, and properties in the mantle transition zone under Bermuda. All of our results are constrained by data from a single seismometer located on the island. Future studies of this region would benefit tremendously from increased instrumentation of the island and the surrounding seafloor.

Data Availability Statement

Data for this study were provided by the IRIS DMC (doi: 10.7914/SN/IU). The computer code developed for this work, rflexa, is available at the archival repository, figshare (doi: 10.6084/m9.figshare.12311870.v1). The authors acknowledge the use of the Generic Mapping Tools (GMT) Version 5.4.4 (Wessel et al., 2013) and the Seismic Analysis Code (SAC) Version 101.6a (Goldstein & Snoke, 2005).

Acknowledgments
This work was partly supported by the U.S. National Science Foundation under grants EAR-1736046 and OCE-1917085, and by Princeton University. High-performance computing resources were provided by the Princeton Institute for Computational Science & Engineering (PICSciE). Thorough and constructive comments by two anonymous reviewers, and by the associate editor, helped us improve the manuscript significantly.

References

Akaogi, M., Takayama, H., Kojitani, H., Kawaji, H., & Atake, T. (2007). Low-temperature heat capacities, entropies and enthalpies of Mg_2SiO_4 polymorphs, and α-β-γ and post-spinel phase relations at high pressure. *Physics and Chemistry of Minerals*, *34*(3), 169–183. https://doi.org/10.1007/s00269-006-0137-3

Ammon, C. J. (1991). The isolation of receiver effects from teleseismic *P* waveforms. *Bulletin of the Seismological Society of America*, *81*, 2504–2510.

Andrews, J., & Deuss, A. (2008). Detailed nature of the 660 km region of the mantle from global receiver function data. *Journal of Geophysical Research*, *113*, B06304. https://doi.org/10.1029/2007JB005111

Becker, J. J., Sandwell, D. T., Smith, W. H. F., Braud, J., Binder, B., Depner, J., et al. (2009). Global bathymetry and elevation data at 30 arc seconds resolution: SRTM30_PLUS. *Marine Geodesy*, *32*(4), 355–371. https://doi.org/10.1080/01490410903297766

Bendat, J. S., & Piersol, A. G. (2000). *Random Data: Analysis and Measurement Procedures* (3rd ed). New York, NY: Wiley.

Benoit, M. H., Long, M. D., & King, S. D. (2013). Anomalously thin transition zone and apparently isotropic upper mantle beneath Bermuda: Evidence for upwelling. *Geochemistry, Geophysics, Geosystems*, *14*(10), 4282–4291. https://doi.org/10.1002/ggge.20277

Bina, C. R., & Helffrich, G. R. (1994). Phase transition Clapeyron slopes and transition zone seismic discontinuity topography. *Journal of Geophysical Research*, *99*(B8), 15853–15860. https://doi.org/10.1029/94JB00462

Cammarano, F., Goes, S., Vacher, P., & Giardini, D. (2003). Inferring upper-mantle temperatures from seismic velocities. *Physics of the Earth and Planetary Interiors*, *138*(3–4), 197–222. https://doi.org/10.1016/S0031-9201(03)00156-0

Chevrot, S., Vinnik, L., & Montagner, J.-P. (1999). Global scale analysis of mantle *Pds* phases. *Journal of Geophysical Research*, *104*(B9), 20203–20219. https://doi.org/10.1029/1999JB900087

Chu, R., Leng, W., Helmberger, D. V., & Gurnis, M. (2013). Hidden hotspot track beneath the eastern United States. *Nature Geoscience*, *6*(11), 963–966. https://doi.org/10.1038/ngeo1949

Cottaar, S., & Deuss, A. (2016). Large-scale mantle discontinuity topography beneath Europe: Signature of akimotoite in subducting slabs. *Journal of Geophysical Research: Solid Earth*, *121*(1), 279–292. https://doi.org/10.1002/2015JB012452

Courtillot, V., Davaille, A., Besse, J., & Stock, J. (2003). Three distinct types of hotspots in the Earth's mantle. *Earth and Planetary Science Letters*, *205*(3–4), 295–308. https://doi.org/10.1016/S0012-821X(02)01048-8

Cox, R. T., & Van Arsdale, R. B. (2002). The Mississippi Embayment, North America: A first order continental structure generated by the Cretaceous superplume mantle event. *Journal of Geodynamics*, *34*(2), 163–176. https://doi.org/10.1016/S0264-3707(02)00019-4

Crotwell, H. P., & Owens, T. J. (2005). Automated receiver function processing. *Seismological Research Letters*, *76*(6), 702–709. https://doi.org/10.1785/gssrl.76.6.702

Crotwell, H. P., Owens, T. J., & Ritsema, J. (1999). The TauP Toolkit: Flexible seismic travel-time and ray-path utilities. *Geophysical Research Letters*, *70*(2), 154–160. https://doi.org/10.1785/gssrl.70.2.154

Davies, D., Kelly, E. J., & Filson, J. R. (1971). Vespa process for analysis of seismic signals. *Nature Physical Science*, *232*(27), 8–13. https://doi.org/10.1038/physci232008a0

Day, E. A., & Deuss, A. (2013). Reconciling *PP* and *P'P'* precursor observations of a complex 660 km seismic discontinuity. *Geophysical Journal International*, *194*(2), 834–838. https://doi.org/10.1093/gji/ggt122

Deuss, A., Redfern, S. A. T., Chambers, K., & Woodhouse, J. H. (2006). The nature of the 660-kilometer discontinuity in Earth's mantle from global seismic observations of *PP* precursors. *Science*, *311*(5758), 198–201. https://doi.org/10.1126/science.1120020

Dueker, K. G., & Sheehan, A. F. (1997). Mantle discontinuity structure from midpoint stacks of converted P to S waves across the Yellowstone hotspot track. *Journal of Geophysical Research*, *102*(B4), 8313–8327. https://doi.org/10.1029/96JB03857

Efron, B., & Tibshirani, R. (1986). Bootstrap methods for standard errors, confidence intervals, and other measures of statistical accuracy. *Statistical Science*, *1*(1), 54–75.

Ekström, G., Nettles, M., & Dziewonski, A. M. (2012). The global CMT project 2004-2010: Centroid-moment tensors for 13,017 earthquakes. *Physics of the Earth and Planetary Interiors*, *200–201*, 1–9. https://doi.org/10.1016/j.pepi.2012.04.002

French, S. W., & Romanowicz, B. (2014). Whole-mantle radially anisotropic shear velocity structure from spectral-element waveform tomography. *Geophysical Journal International*, *199*(3), 1303–1327. https://doi.org/10.1093/gji/ggu334

French, S. W., & Romanowicz, B. (2015). Broad plumes rooted at the base of the Earth's mantle beneath major hotspots. *Nature*, *525*(7567), 95–99. https://doi.org/10.1038/nature14876

Frost, D. J. (2008). The upper mantle and transition zone. *Elements*, *4*(3), 171–176. https://doi.org/10.2113/GSELEMENTS.4.3.171
Gao, S. S., & Liu, K. H. (2014). Mantle transition zone discontinuities beneath the contiguous United States. *Journal of Geophysical Research*, *119*(8), 6452–6468. https://doi.org/10.1002/2014JB011253
Goldstein, P., & Snoke, A. (2005). In: SAC Availability for the IRIS Community. Incorporated Research Institutions for Seismology newsletter (7) UCRL-JRNL-211140.
Gurrola, H., Minster, J. B., & Owens, T. (1994). The use of velocity spectrum for stacking receiver functions and imaging upper mantle discontinuities. *Geophysical Journal International*, *117*(2), 427–440. https://doi.org/10.1111/j.1365-246X.1994.tb03942.x
Helffrich, G. R. (2000). Topography of the transition zone seismic discontinuities. *Reviews of Geophysics*, *38*(1), 141–158. https://doi.org/10.1029/1999RG000060
Helffrich, G. R., Asencio, E., Knapp, J., & Owens, T. (2003). Transition zone structure in a tectonically inactive area: 410 and 660 km discontinuity properties under the northern North Sea. *Geophysical Journal International*, *155*(1), 193–199. https://doi.org/10.1046/j.1365-246X.2003.02036.x
Helffrich, G. R., & Wood, B. J. (2001). The Earth's mantle. *Nature*, *412*(6846), 501–507. https://doi.org/10.1038/35087500
Hirose, K. (2002). Phase transitions in pyrolitic mantle around 670-km depth: Implications for upwelling of plumes from the lower mantle. *Journal of Geophysical Research*, *107*(B4), 2078. https://doi.org/10.1029/2001JB000597
Houser, C., & Williams, Q. (2010). Reconciling Pacific 410 and 660 km discontinuity topography, transition zone shear velocity patterns, and mantle phase transitions. *Earth and Planetary Science Letters*, *296*(3–4), 255–266. https://doi.org/10.1016/j.epsl.2010.05.006
Ito, E., Akaogi, M., Topor, L., & Navrotsky, A. (1990). Negative pressure-temperature slopes for reactions forming $MgSiO_3$ perovskite from calorimetry. *Science*, *249*(4974), 1275–1278. https://doi.org/10.1126/science.249.4974.1275
Jenkins, J., Cottaar, S., White, R. S., & Deuss, A. (2016). Depressed mantle discontinuities beneath Iceland: Evidence of a garnet controlled 660 km discontinuity?. *Earth and Planetary Science Letters*, *433*, 159–168. https://doi.org/10.1016/j.epsl.2015.10.053
Kennett, B. L. N., & Engdahl, E. R. (1991). Travel times for global earthquake location and phase identification. *Geophysical Journal International*, *105*(2), 429–465. https://doi.org/10.1111/j.1365-246X.1991.tb06724.x
Kind, R., & Vinnik, L. P. (1988). The upper-mantle discontinuities underneath the GRF array from *P*-to-*S* converted phases. *Journal of Geophysics*, *62*(1), 138–147.
King, S. D., & Adam, C. (2014). Hotspot swells revisited. *Physics of the Earth and Planetary Interiors*, *235*, 66–83. https://doi.org/10.1016/j.pepi.2014.07.006
Langston, C. A. (1979). Structure under Mount Rainier, Washington, inferred from teleseismic body waves. *Journal of Geophysical Research*, *84*(B9), 4749–4762. https://doi.org/10.1029/JB084iB09p04749
Lawrence, J. F., & Shearer, P. M. (2006). A global study of transition zone thickness using receiver functions. *Journal of Geophysical Research*, *111*(B06307). https://doi.org/10.1029/2005JB003973
Leahy, G. M. (2009). Local variability in the 410-km mantle discontinuity under a hotspot. *Earth and Planetary Science Letters*, *288*(1–2), 158–163. https://doi.org/10.1016/j.epsl.2009.09.018
Lekić, V., Cottaar, S., Dziewoński, A., & Romanowicz, B. (2012). Cluster analysis of global lower mantle tomography: A new class of structure and implications for chemical heterogeneity. *Earth and Planetary Science Letters*, *357*, 68–77. https://doi.org/10.1016/j.epsl.2012.09.014
Ligorría, J. P., & Ammon, C. J. (1999). Iterative deconvolution and receiver-function estimation. *Bulletin of the Seismological Society of America*, *89*(5), 1395–1400.
Liu, K. H., & Gao, S. S. (2006). Mantle transition zone discontinuities beneath the Baikal rift and adjacent areas. *Journal of Geophysical Research*, *111*(B11301). https://doi.org/10.1029/2005JB004099
Liu, L., Gao, S. S., Liu, K. H., & Mickus, K. (2017). Receiver function and gravity constraints on crustal structure and vertical movements of the Upper Mississippi Embayment and Ozark Uplift. *Journal of Geophysical Research*, *122*(6), 4572–4583. https://doi.org/10.1002/2017JB014201
Mazza, S. E., Gazel, E., Johnson, E. A., Kunk, M. J., McAleer, R., Spotila, J. A., et al. (2014). Volcanoes of the passive margin: The youngest magmatic event in eastern North America. *Geology*, *42*(6), 483–486. https://doi.org/10.1130/G35407.1
Morgan, W. J. (1971). Convection plumes in the lower mantle. *Nature*, *230*(5288), 42–43. https://doi.org/10.1038/230042a0
Nissen-Meyer, T., van Driel, M., Stähler, S. C., Hosseini, K., Hempel, S., Auer, L., et al. (2014). AxiSEM: Broadband 3-D seismic wavefields in axisymmetric media. *Solid Earth*, *5*, 425–445. https://doi.org/10.5194/se-5-425-2014
Phinney, R. A. (1964). Structure of the Earth's crust from spectral behavior of long-period body waves. *Journal of Geophysical Research*, *69*(14), 2997–3017. https://doi.org/10.1029/JZ069i014p02997
Shearer, P. M. (1990). Seismic imaging of upper-mantle structure with new evidence for a 520-km discontinuity. *Nature*, *334*(6262), 121–126. https://doi.org/10.1038/344121a0
Sigloch, K., McQuarrie, N., & Nolet, G. (2008). Two-stage subduction history under North America inferred from multiple-frequency tomography. *Nature Geoscience*, *1*(7), 458–462. https://doi.org/10.1038/ngeo231
Simmons, N. A., & Gurrola, H. (2000). Multiple seismic discontinuities near the base of the transition zone in the Earth's mantle. *Nature*, *405*(6786), 559–562. https://doi.org/10.1038/35014589
Simmons, N. A., Myers, S. C., Johannesson, G., Matzel, E., & Grand, S. P. (2015). Evidence for long-lived subduction of an ancient tectonic plate beneath the southern Indian Ocean. *Geophysical Research Letters*, *42*(21), 9270–9278. https://doi.org/10.1002/2015GL066237
Sleep, N. H. (1990). Hotspots and mantle plumes: Some phenomenology. *Journal of Geophysical Research*, *95*(B5), 6715–6736. https://doi.org/10.1029/JB095iB05p06715
Steinberger, B., Sutherland, R., & O'Connell, R. J. (2004). Prediction of Emperor-Hawaii seamount locations from a revised model of global plate motion and mantle flow. *Nature*, *430*, 167–173. https://doi.org/10.1038/nature02660
Tauzin, B., Debayle, E., & Wittlinger, G. (2008). The mantle transition zone as seen by global Pds phases: No clear evidence for a thin transition zone beneath hotspots. *Journal of Geophysical Research*, *113*(B08309). https://doi.org/10.1029/2007JB005364
Tsujino, N., Yoshino, T., Yamazaki, D., Sakurai, M., Sun, W., Xu, F., et al. (2019). Phase transition of wadsleyite-ringwoodite in the Mg_2SiO_4-Fe_2SiO_4 system. *American Mineralogist*, *104*, 588–594. https://doi.org/10.2138/am-2019-6823
Vacher, P., Mocquet, A., & Sotin, C. (1998). Computation of seismic profiles from mineral physics: The importance of the non-olivine components for explaining the 660 km depth discontinuity. *Physics of the Earth and Planetary Interiors*, *106*(3), 275–298. https://doi.org/10.1016/S0031-9201(98)00076-4
van der Meijde, M., Marone, F., Giardini, D., & van der Lee, S. (2003). Seismic evidence for water deep in Earth's upper mantle. *Science*, *300*(5625), 1556–1558. https://doi.org/10.1126/science.1083636

van Driel, M., Krischer, L., Stähler, S., Hosseini, K., & Nissen-Meyer, T. (2015). Instaseis: Instant global seismograms based on a broadband waveform database. *Solid Earth*, *6*(2), 701–717. https://doi.org/10.5194/se-6-701-2015

Vinnik, L. (1977). Detection of waves converted from P to SV in the mantle. *Physics of the Earth and Planetary Interiors*, *15*(1), 39–45. https://doi.org/10.1016/0031-9201(77)90008-5

Vogt, P., & Jung, W.-Y. (2007). Origin of the Bermuda volcanoes and the Bermuda Rise: History, observations, models, and puzzles. *Geological Society of America Special Paper*, *430*, 553–591. https://doi.org/10.1130/SPE430

Wessel, P., Smith, W. H. F., Scharroo, R., Luis, J., & Wobbe, F. (2013). Generic Mapping Tools: Improved version released. *Eos, Transaction American Geophysical Union*, *94*(45), 409–410. https://doi.org/10.1002/2013EO450001

Yang, X., Pavlis, G. L., & Wang, Y. (2016). A quality control method for teleseismic *P*-wave receiver functions. *Bulletin of the Seismological Society of America*, *106*(5), 1948–1962. https://doi.org/10.1785/0120150347

Yu, Y., Song, J., Liu, K. H., & Gao, S. S. (2015). Determining crustal structure beneath seismic stations overlying a low-velocity sedimentary layer using receiver functions. *Journal of Geophysical Research: Solid Earth*, *120*(5), 3208–3218. https://doi.org/10.1002/2014JB011610

Zelt, B. C., & Ellis, R. M. (1999). Receiver-function studies in the Trans-Hudson orogen, Saskatchewan. *Canadian Journal of Earth Sciences*, *36*(4), 585–603. https://doi.org/10.1139/e98-109